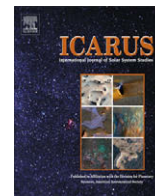




Contents lists available at ScienceDirect

Icarus

journal homepage: www.elsevier.com/locate/icarus

Thermal tides on Pluto

Anthony D. Toigo^{a,*}, Peter J. Gierasch^b, Bruno Sicardy^c, Emmanuel Lellouch^c

^aCenter for Radiophysics and Space Research, Cornell University, Ithaca, NY 14853-6801, United States

^bAstronomy Department, Cornell University, Ithaca, NY 14853-6801, United States

^cLESIA, Observatoire de Paris, 5 place Jules Janssen, 92195 Meudon, France

ARTICLE INFO

Article history:

Received 31 July 2009

Revised 19 January 2010

Accepted 25 January 2010

Available online xxx

Keywords:

Pluto, Atmosphere

Tides, Atmospheric

Occultations

Pluto

Atmospheres, Structure

ABSTRACT

Stellar occultations have shown that vertical profiles of density fluctuations in the atmosphere of Pluto typically show wave-like structure with an amplitude of a few percent and vertical wavelengths of a few kilometers. Here we calculate the tidal response of Pluto's atmosphere to solar-induced sublimation "breathing" from N₂ frost patches. Solutions show global-scale wave-like density structure capable of explaining the observations. The atmospheric response is a combination of eastward and westward migrating tides, together with a zonally symmetric mode. Calculated vertical wavelengths and amplitudes are similar to observations.

© 2010 Elsevier Inc. All rights reserved.

1. Introduction

There is evidence from stellar occultations that Pluto's atmosphere is layered, with oscillations in the vertical profile of its temperature, $T(z)$ (Sicardy et al., 2003; Pasachoff et al., 2005; McCarthy et al., 2008; Person et al., 2008). The amplitude is a few degrees with dominant wavelengths of approximately 8 and 12 km. The perturbations are superposed on a mean middle atmosphere temperature of about 100 K (Sicardy et al., 2003; Elliot et al., 2007). There is evidence that the perturbations are global in scale, and Pasachoff et al. (2005), McCarthy et al. (2008), and Person et al. (2008) propose that they are due to atmospheric waves. They do not, however, put forward any particular forcing mechanism. Here we calculate the atmospheric tides forced by diurnal variations of N₂ sublimation and show that they can explain the observations.

The basic state of Pluto's middle atmosphere, as shown in Fig. 1, is close to isothermal at around 100 K, with temperature higher than that of a black body at equilibrium with sunlight, which would be about 40 K. Infrared observations show that the mean surface temperature \bar{T}_s is about 47–52 K (Lellouch et al., 2000), implying that radiative cooling of the atmosphere is inefficient. The nature of the transition zone between warm middle atmosphere and cold surface is a subject of some uncertainty (Lellouch, 1994), since the cold base of the atmosphere may lead to haze formation. For purposes of studying atmospheric dynamics, the

important point is that a near-surface inversion exists, with thickness of about a scale height or less.

Detailed modeling leads to a complicated description of Pluto's surface (Lellouch et al., 2000), partially covered with patches of N₂ ice. The atmosphere is thought to be mostly N₂, with a small amount of methane. The surface N₂ ice controls the atmospheric pressure, which can vary on seasonal time scales in complicated ways as the mean surface temperature and amount of N₂ ice exposed to the view of sunlight vary (Hansen and Paige, 1996; Lellouch et al., 2009). The current surface pressure is thought to lie between about 0.7 and 2.4 Pa (Hansen and Paige, 1996; Elliot et al., 2003; Sicardy et al., 2003; Lellouch et al., 2009).

There are infrared measurements indicating a diurnal variation of surface temperature, however (Lellouch et al., 2000). This observation is not consistent with vapor pressure buffering of temperatures, and supports the conclusion by Lellouch et al. (2000) that the surface is patchy, with areas of exposed N₂ ice buffering the long-term surface pressure and temperature, and areas of soil showing a diurnal variation of temperature. Hubble Space Telescope (Stern et al., 1997) and ground-based (Young et al., 1999, 2001) observations of Pluto–Charon mutual occultations have led to detailed albedo maps of Pluto's surface (see Fig. 2).

2. Layered density structures and waves

The layered atmospheric structure may be produced by waves driven by the surface response to diurnal solar heating variations, but not through direct heating by radiation. The radiative time

* Corresponding author. Present address: Johns Hopkins University, Applied Physics Laboratory, Laurel, MD 20723, United States.

E-mail address: toigo@astro.cornell.edu (A.D. Toigo).

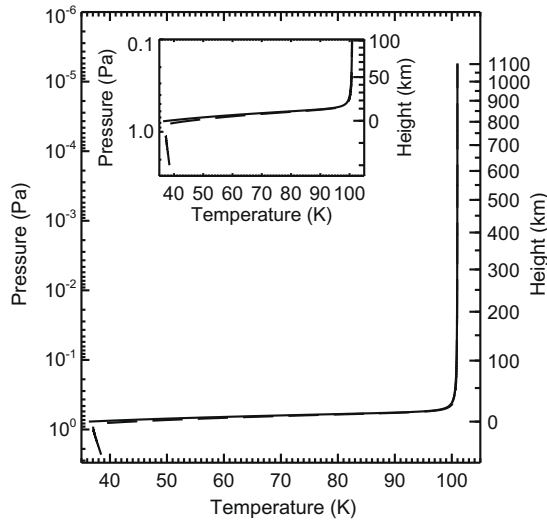


Fig. 1. Temperature of Pluto's atmosphere as a function of pressure for two bracketing cases, one with a high surface pressure, approximately 2.3 Pa, drawn with a dashed line, and the other with a low surface pressure, approximately 0.77 Pa, drawn with a solid line. These two bracketing cases represent extremes of that base state that are also still consistent with both occultation and spectral results. The two profiles are almost identical except for the extra downward extension to the profile in the high surface pressure case. The inset graph shows a zoomed-in area of the plot near the surface, with its large temperature gradient, and showing the main differences between the two bracketing cases. Most results from the tidal calculations shown in the later figures use the low surface pressure profile since this gives larger temperature oscillations. Heights on the right-hand y-axis for both plots are approximate, are based on the low surface pressure profile, and are merely included for ease of reference.

constant of the atmosphere itself is extremely long (Strobel et al., 1996), and it is not possible for atmospheric oscillations to respond directly to day–night heating variations. Estimates by Strobel et al. (1996) give time constants on the order of a decade, implying a diurnal fractional radiative response of approximately 2×10^{-3} , or 0.2 K. The surface temperature varies diurnally, at least in areas

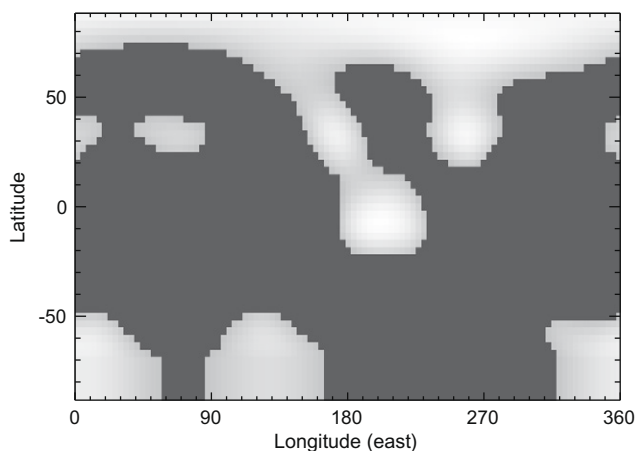


Fig. 2. Albedo map of Pluto, from Stern et al. (1997), which has been converted into a “frost map function”, $M(\lambda, \phi)$, by assuming that only locations with an albedo higher than a critical value, A_0 , had N_2 ice deposits on the surface. The critical value used for A_0 was 0.7. The plot shows the convolution of the albedo and frost maps, such that black indicates that the location has no N_2 ice, and thus does not contribute to the surface forcing function (w_s , the boundary condition on w at the surface), while the brightness of the white color is proportional to the albedo value used when calculating surface insolation flux contributing to w_s , ranging from $A_0(=0.7)$ to 1.0. Longitude increases eastward, and the convention of the direction of the angular momentum vector as defining local north, rather than the IAU ecliptic-based definition, has been adopted.

Table 1
Numbers used in calculations.

Symbol	value	Description	References
a	1182 km (1162–1202 km)	Radius of Pluto	1
g	0.623 m s^{-2}	Acceleration of gravity	1 and 2
Ω	$1.13856 \times 10^{-5} \text{ s}^{-1}$	Rotation rate	3
R	$296.8 \text{ J kg}^{-1} \text{ K}^{-1}$	Gas constant, N_2	4
c_p	$3.5R$	Specific heat, N_2	4
γ	$7/5$	Ratio of specific heats	4
L	$2.48 \times 10^5 \text{ J kg}^{-1}$	Latent heat, N_2 at 40 K	4
\bar{T}_{s,N_2}	40 K	Temperature of surface N_2 ice	5
P_s	0.77 Pa (0.7–2.4 Pa)	Surface pressure	6
δ_\odot	29°	Declination of the Sun at Pluto	7
F_\odot	1.47 W m^{-2}	Solar flux at Pluto	7 and 8

References – (1) Sicardy et al. (2003) and Lellouch et al. (2009) for the range, while the arithmetic mean was chosen for the tidal calculations; (2) Tholen et al. (2008) for GM of Pluto; (3) Tholen et al. (2008); (4) Lide (2008); (5) Tryka et al. (1994); (6) Lellouch et al. (2000), where a surface pressure of 0.77 Pa was chosen in the tidal calculations to replicate the conditions of the 2002 observations of Sicardy et al. (2003); (7) JPL HORIZONS on-line Solar System data and ephemeris computation service, <<http://ssd.jpl.nasa.gov/?horizons>>, where the period of the 2002 observations of Sicardy et al. (2003) was used. Additionally, we adopt the convention of the direction of the angular momentum vector as defining local north, rather than the IAU ecliptic-based definition, and so our declination is a positive angle; (8) The value of the solar flux at Pluto was calculated from the solar flux at Earth, 1367.6 W m^{-2} (Lodders and Fegley, 1998), and the distance of Pluto from the Sun at the time of observations of Sicardy et al. (2003), approximately 30.5 AU, taken from the JPL HORIZONS system.

not buffered by frost, but this also can have only a small direct effect on the atmosphere as the radiative coupling is weak. The presence of a strong inversion within the lowest scale height (Sicardy et al., 2003) will prevent convective heat transport, and making it unlikely that a deep convective boundary layer will develop near local noon. Thus we expect neither convection nor direct radiative forcing to be of any significance for driving global tidal oscillations.

Here we investigate the possibility that there are tidal waves in Pluto's atmosphere driven, instead, by the diurnal variations in N_2 sublimation within the patches of surface that are covered in N_2 ice. A rough estimate of the vertical velocity amplitude due to sublimation forcing can be made by equating the latent heat flux with the insolation flux. At local noon an icy N_2 patch will sublimate and produce a vertical gas velocity

$$w \sim \frac{(1-A)F_\odot}{\rho L}, \quad (1)$$

where A is the albedo of the icy N_2 surface, F_\odot is the solar flux, ρ is the gas density, and L is the latent heat of sublimation for N_2 . Replacing ρ through the ideal gas law and using estimates for the various parameters gives

$$w \sim \frac{(1-A)F_\odot R \bar{T}_{s,N_2}}{P_s L} \sim 2.7 \times 10^{-2} \text{ m/s}, \quad (2)$$

where \bar{T}_{s,N_2} is the temperature of the surface N_2 ice patch and values from Table 1 and a minimum N_2 ice albedo of 0.7 (see below) have been used. It can also be seen that the vertical gas velocity, and thus the surface forcing of waves, is inversely proportional to the surface pressure, for which there is still some uncertainty. Larger surface pressures will produce smaller vertical velocities, and thus decrease the wave forcing.

The angular rotation rate of the Pluto–Charon system is $\Omega = 1.13856 \times 10^{-5} \text{ s}^{-1}$ (Tholen et al., 2008). The vertical displacement of parcels, δ , can be estimated to be on the order of $w/\Omega \sim 2.4$ km, enough to produce temperature perturbations of about $g\delta/c_p \sim 1.4$ K. This is large enough to be of interest to stellar occultation observers.

3. Tidal model

We utilize a standard classical tidal model to explore atmospheric oscillations. The standard classical tidal model makes the “thin atmosphere” assumption, which assumes that an atmospheric scale height is much less than the planetary radius. For Pluto, this is a less accurate assumption as a scale height is approximately 4–5% of the planetary radius, and thus the variations of gravity, g , should be taken into account. However, while the solutions to a more thorough tidal solution would take the variation of g into account, we believe the standard classical tidal model provides a good approximation to the true tidal response as well as being a good qualitative descriptor of the pattern of oscillations.

We seek solutions to the “forced” equations (rather than the free oscillations solution) because of the surface boundary condition, expressed as a “breathing” of the frost surfaces forced by the diurnal cycle. The vertical velocity, w , at the surface can be written

$$w_S(\lambda, \phi, t) = [1 - A(\lambda, \phi)] \frac{F'(\lambda, \phi, t)}{\rho_S L} M(\lambda, \phi), \quad (3)$$

where λ , ϕ , and t are longitude, latitude, and time, respectively, a subscript S indicates a surface value, A is the (spatially-variable) albedo, F' is the diurnal thermal forcing (with diurnal mean removed), and the frost map function, M , is unity where frost exists and zero where the soil is bare. The frost map function, convolved with the albedo map, that we used, derived from a Hubble Space Telescope image of Pluto, is displayed in Fig. 2. The simplifying assumption was that for any part of the planet that was darker than a critical “cutoff” albedo of A_0 , there was no N_2 ice, and vice versa. The net sublimation mass flux will vary during the diurnal cycle in a complicated way because of the longitudinal variations of M , and at certain times there may be a net pumping of mass into the atmosphere. The oscillating mass transport into the atmosphere, however, is small compared with the total atmospheric mass, and the mean surface pressure remains constant to a first approximation. This is shown by the estimate

$$\frac{\Delta P}{P} \sim \frac{g(1 - A_0)F'}{L\Omega P_S} f_A \sim 10^{-2}, \quad (4)$$

where f_A is the areal fraction of the planet that is covered in exposed N_2 ice patches, which is about 0.2 for our assumption of a cutoff albedo, A_0 , of 0.7, and F' is the magnitude of the diurnal variations in insolation (defined in Eq. (A16) below). More accurate surface ice maps than that which we have used will not significantly change our results qualitatively, as the tidal response at higher wavenumbers than the diurnal forcing is significantly reduced, and thus more accurate maps would only contribute power to surface forcing components where there would be limited response.

Eq. (3) is the sole drive for the motions we study, since radiative forcing is weak and convective activity is damped. Eq. (3) then becomes our bottom boundary condition. We shall further assume that energy is not reflected downward from the upper atmosphere. Details of the tidal equations and the method of their solution are described in Appendix A.

4. Numerical results

We seek *forced* solutions to the linearized tidal equations (described in more detail in Appendix A, q.v.). The forcing is from the diurnal oscillation of insolation as expressed through the surface flux of sublimating N_2 gas as described in Section 3 above. For the results we present here, we have retained only the diurnal frequency even though higher frequencies are excited by a realistic mathematical description of the insolation. Specifically, we approximated the

surface heating function as a two term combination of a constant and a harmonic of diurnal frequency with amplitude equal to half of the daily maximum insolation. This approach retained the important qualitative features of the tides while considerably simplifying the computation of solutions.

Numerical solutions for the tidal equations were created for each eigenvalue for a given longitudinal wavenumber, s , and frequency, σ , of forcing up to about 20 eigenvalues for each longitudinal wavenumber. The eigenvalues were organized and recorded as positive or negative, and symmetric or antisymmetric. The solutions were then summed over all (20 or so) eigenvalues and all longitudinal wavenumbers (for the range -5 to 5 where there was significant power in the forcing function), and the results for the low surface pressure profile of Fig. 1 are shown in Figs. 3–7.

Regions of large wave amplitude are mostly confined to near-equatorial latitudes, at heights near the surface (where the temperature gradient is very large) or large heights (where the exponential growth of the waves becomes significant). The subtle structure seen at mid- and high-latitudes (e.g., Fig. 4) is due almost entirely to the $s = 0$ (zonally uniform) longitudinal wavenumber component. This wavenumber has significant power due to the relatively large power in the $s = -1$ component of the surface N_2 ice distribution function, $M(\lambda, \phi)$, convolved with the diurnal solar forcing function, with its component of $s = 1$.

Vertical profiles of temperature perturbation for a few selected positions and for both extremes of low and high surface pressure cases are shown in Fig. 7, and the Fourier transform of those profiles is shown in Fig. 8, where it can be seen that the strongest vertical wavelengths for all cases and locations are approximately 8 and 12 km. These dominant wavelengths arise from specific eigenvalues that represent surface forcing components with the largest coefficients. The two most strongly forced eigenmodes are the lowest antisymmetric mode for longitudinal wavenumber 0 and the lowest symmetric mode for longitudinal wavenumber 1. These two modes display wavelengths of 12 and 7.7 km.

Although the numerical calculations presented in Figs. 3–7 show the amplitudes increasing exponentially with height, the linearization of the fundamental equations used to make the

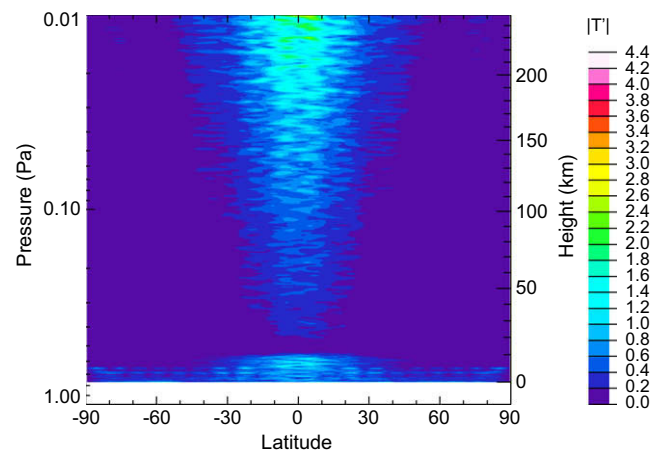


Fig. 3. Amplitude of the sum of all diurnal gravity wave modes (all positive and negative symmetric and antisymmetric eigenvalues for all positive and negative values of the longitudinal wavenumber, s , between -5 and 5) as a function of latitude and pressure. The “amplitude” of the gravity waves here, $|T'(\phi, z)|$, is actually $\sqrt{2}$ times the average deviation from the mean, that is, $|T'(\phi, z)| = \sqrt{2 \int_{-\pi}^{\pi} (T'(\lambda, \phi, z) - \bar{T}'(\phi, z))^2 d\lambda}$, where $\bar{T}'(\lambda, z) = \frac{1}{2\pi} \int_{-\pi}^{\pi} T'(\lambda, \phi, z) d\lambda$. The $\sqrt{2}$ factor comes from trying to match the average deviation from the mean to the amplitude of a single wavelength sine wave. Since the only source of forcing is the diurnal heating, an implicit $e^{-i\omega t}$ is assumed to multiply all terms. Height on the right-hand y-axis is approximate and is included for ease of reference.

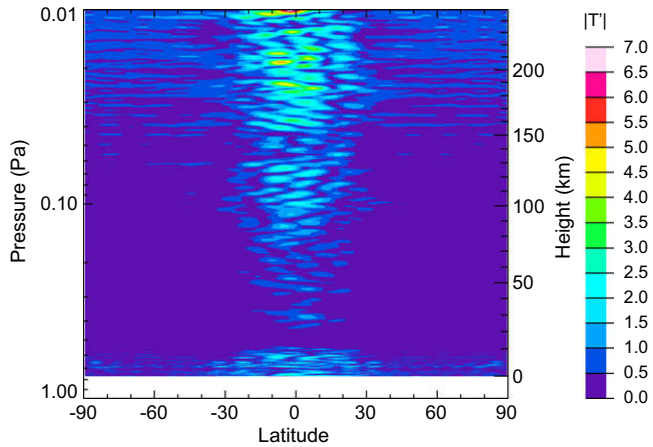


Fig. 4. Amplitude of the sum of all gravity wave modes (same sum as described in Fig. 3) as a function of latitude and pressure, for oscillations at longitude 200°E . Here the amplitude of the gravity waves, $|T'(\lambda = 200^\circ\text{E}, \phi, z)|$, is evaluated at a specific longitude and thus the perturbation temperature, T' , will oscillate around zero perturbation with a frequency of Ω , i.e., $T' = |T'|e^{-i\Omega t}$. The longitude 200°E was chosen because it is a longitude that is expected to be experiencing large forcing, based on the N_2 ice distribution map used and shown in Fig. 2. Height on the right-hand y-axis is approximate and is included for ease of reference.

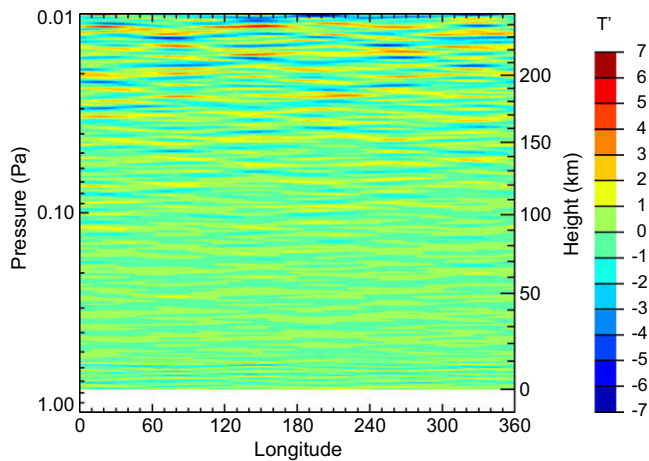


Fig. 5. Amplitude of the sum of all diurnal gravity wave modes (all positive and negative symmetric and antisymmetric eigenvalues for all positive and negative values of the longitudinal wavenumber, s , between -5 and 5) as a function of longitude and pressure, at the equator and at an instant of time where the local time at 180°E is noon. The equator is where the strongest amplitudes with respect to latitude occur (see Fig. 3). Height on the right-hand y-axis is approximate and is included for ease of reference.

calculations will break down at high elevations, where both convective and shear instabilities are expected. The resulting deposition of momentum and energy may produce important mean flows. In addition, the turbulence produced by instabilities may contribute to the refractive perturbations detected during occultations. It might at first sight appear impossible for turbulence to produce the lateral coherence shown by occultations (e.g., McCarthy et al., 2008), but if the observed layers are remnants of turbulence produced by organized waves, the layers might retain the pattern of the wave well after its passage. Layers of turbulence are common in the terrestrial lower stratosphere, where vertically propagating waves produce pancake-shaped patches of nearly adiabatic overturning. The patches are thought to be produced by wave breaking, and survive after the wave has passed (Kelley et al., 2002). Terrestrial turbulence patches are usually of a smaller scale than would be observable in occultations of the Earth, but the

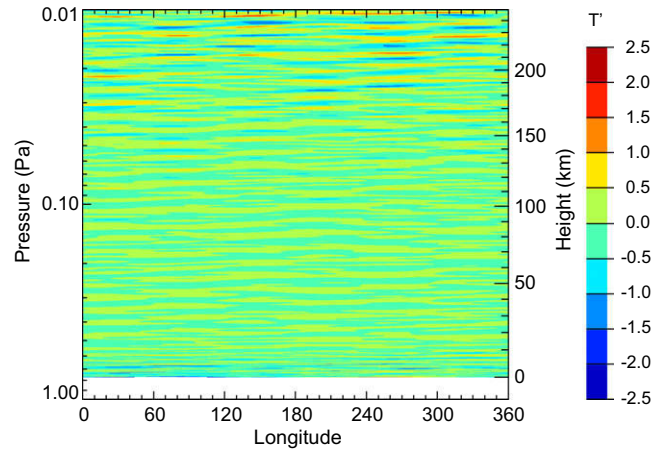


Fig. 6. Amplitude of the sum of all diurnal gravity wave modes (all positive and negative symmetric and antisymmetric eigenvalues for all positive and negative values of the longitudinal wavenumber, s , between -5 and 5) as a function of longitude and pressure, at latitude 30°N and at an instant of time where the local time at 180°E is noon. 29°N is the declination of the Sun, and so 30°N represents approximately the latitude of largest mean heating, although amplitudes of diurnal oscillations are still less than at the equator. Height on the right-hand y-axis is approximate and is included for ease of reference.

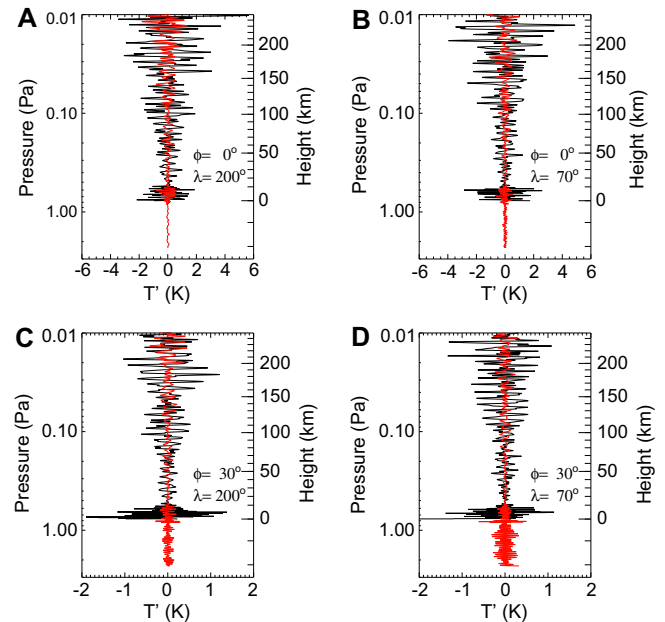


Fig. 7. Temperature perturbation profiles as a function of pressure and height at four selected locations. The latitudes chosen are the equator and 30°N , the same latitudes as used in Figs. 5 and 6, while the longitudes chosen are 200°E and 70°E . 200°E was selected as a representative location of strong forcing, and was also the longitude used in Fig. 4. 70°E was selected as a representative location of weak forcing, being in a large relatively N_2 ice-free region, as seen in Fig. 2. The black line shows our standard low surface pressure case, and the red line shows for comparison calculations made with the high surface pressure case shown in Fig. 1. Local time is noon for each profile. Height on the right-hand y-axis is approximate and is included for ease of reference. Despite the difference in surface ice coverage at the two different longitudes, the difference in wave amplitudes is not particularly large, indicating that at any particular location, the wave amplitudes are more dominated by the constructive and destructive interference of wave modes than by direct forcing from the surface below. (A) Equator, 200°E . (B) Equator, 70°E . (C) 30°N , 200°E . (D) 30°N , 70°E .

production of waves on Pluto may be of larger scale, particularly if they are forced by tides.

Molecular viscosity may also be important in damping the tidal waves at high elevations. When the frictional damping term (due

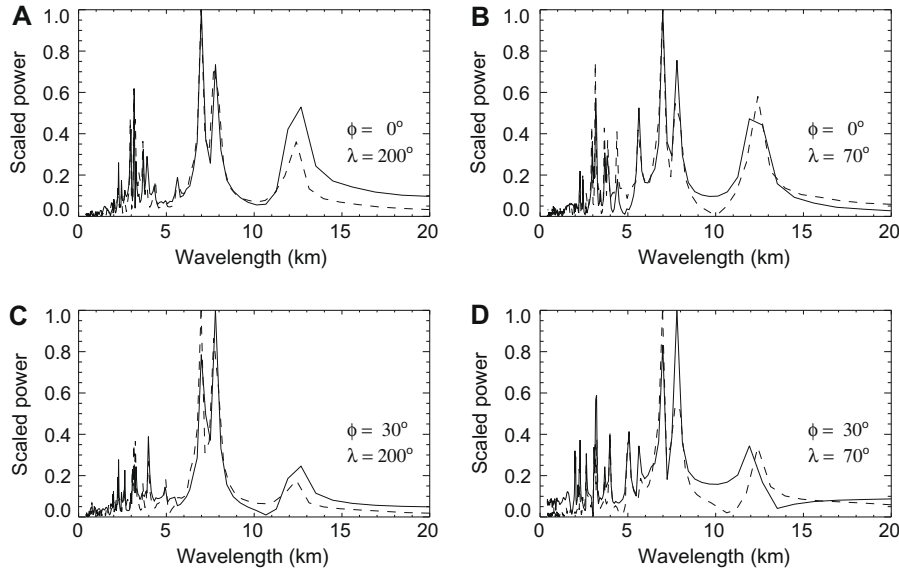


Fig. 8. Fourier transforms of the vertical profiles in Fig. 7. Power is scaled so that the maximum value for the plotted range is always 1. The solid line shows our standard low surface pressure case, while the dashed line shows for comparison analysis of the high surface pressure case profiles shown in Fig. 7. At all four sampled locations, power can be seen in essentially the same dominant wavelengths (i.e., approximately 7–8 km and 12 km), with only the relative magnitude varying. (A) Equator, 200°E. (B) Equator, 70°E. (C) 30°N, 200°E. (D) 30°N, 70°E.

to molecular viscosity) in the momentum equation becomes the same order of magnitude as the time rate of change term, we expect the waves to start breaking and stop propagating. Using the kinematic molecular viscosity, ν , this condition will occur when

$$\nu \frac{\partial^2 u}{\partial z^2} \sim \frac{\nu}{(\Delta z)^2} U,$$

is of the same order as

$$\frac{\partial u}{\partial t} \sim \Omega U,$$

or, equivalently, when

$$\nu \geq \Omega (\Delta z)^2, \quad (5)$$

where U is the scale of typical east–west wind, Δz is the scale for typical changes in the east–west wind, and changes in time are assumed to occur at the diurnal frequency, Ω . Assuming that the dynamic viscosity, $\mu (= \rho \nu)$, is only a function of temperature and that dependence is $\mu \propto T^{1/2}$, the kinematic viscosity is thus proportional to both T and ρ , or taking advantage of the equation of state, that $\nu \propto T^{3/2} P^{-1}$. If we write

$$\nu = \nu_{STP} \left(\frac{T}{T_{STP}} \right)^{3/2} \left(\frac{P_{STP}}{P} \right), \quad (6)$$

we can combine Eqs. (5) and (6) to solve for the pressure at which molecular viscosity will become important for damping wave amplitudes:

$$P \geq \frac{P_{STP} \nu_{STP}}{\Omega (\Delta z)^2} \left(\frac{T}{T_{STP}} \right)^{3/2} \sim 10^{-2} \text{ Pa}. \quad (7)$$

Here, the kinematic viscosity of N_2 at room temperature and pressure, ν_{STP} , is about $1.5 \times 10^{-5} \text{ m}^2 \text{ s}^{-1}$ (Lide, 2008), room temperature, T_{STP} , is about 293 K, room pressure, P_{STP} , is about $1.01325 \times 10^5 \text{ Pa}$, and we have set Δz to be the inverse of the angular wavenumber of vertical oscillations, i.e., $\Delta z \sim 1/\kappa = \lambda/2\pi$, where a wavelength of order 10 km was used. Thus absorption of tidal

wave energy should begin near four scale heights, and should grow in importance above this height. Figs. 3–7 only show up to about 10^{-2} Pa for this reason.

The dominant wavelengths of temperature perturbations implied by the spikes in the occultation light curves are in good agreement with predictions of the tidal calculations. Examples of a synthetic light curve, along with an sample observation for comparison, are displayed in Fig. 9. These synthetic light curves were generated with the plane parallel atmosphere approximation, which should be adequate for atmospheric structures whose horizontal variation is of global scale. The light curve is based on the temperature profile shown in Fig. 7A, which was a region with significant frost cover, and thus relatively large forcing. This synthetic light curve based on our tidal calculations agrees well with the observational light curve also shown in Fig. 9 (top and bottom) in the bright portion of the light curve where the plane parallel approximation is most valid, but only after reducing the atmospheric temperature oscillations by a factor of 3–4 (Fig. 9, bottom). We have chosen for our standard case (and shown in the figures in this article) the low extreme of expected surface pressures, and have thus predicted the high extreme of surface forcing and wave amplitudes as per Eq. (2). A reduction of wave amplitudes by a factor of 3–4 is consistent with the use of a different surface pressure within the range of uncertainty (Hansen and Paige, 1996; Sicardy et al., 2003; Lellouch et al., 2009).

We also conducted calculations using a different N_2 surface ice distribution map to determine its effect on the nature of the atmospheric waves. The alternate N_2 surface ice distribution map was taken from Lellouch et al. (2000), and is labeled as the “Modified Grundy and Fink’ model” in Fig. 6 of that paper, but also as the “Lellouch et al. (2000) map” in Fig. 10 of Grundy and Buie (2001). This alternate map had over twice the surface N_2 ice as the original map we used in our calculations, approximately 63% of the surface as compared to 24%. However, despite this difference in total surface N_2 ice coverage, no significant qualitative difference in the behavior or nature of the atmospheric waves was noticed, apart from slightly higher wave amplitudes (approximately 20–50% depending on location and altitude) and moderately less power seen at the 12 km vertical wavelength. We do not show the results here, since, except for

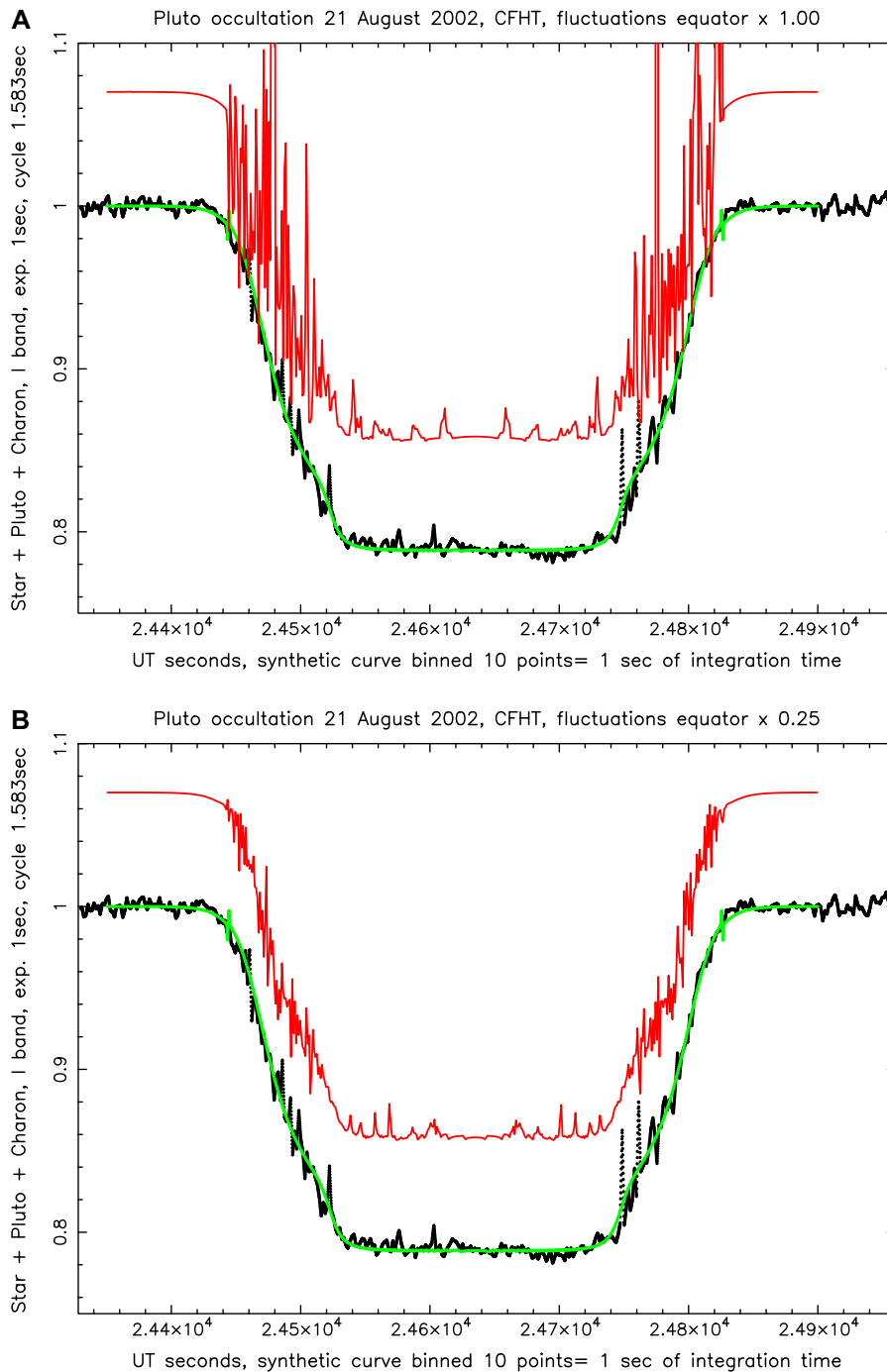


Fig. 9. Synthetic light curves made from the calculated temperature profile shown in Fig. 7A plotted on top of an observed light curve from the August 21, 2002 stellar occultation by Pluto, observed from the 3.55-m Canada–France–Hawaii Telescope (CFHT) in Hawaii (Sicardy et al., 2003). The observation is in black. A synthetic light curve derived from the smoothed profiles shown in Fig. 1 is shown in green. A synthetic light curve from our tidal calculations of the low surface pressure case is shown in red (and shifted upward to more easily be seen). The synthetic profiles were smoothed over the Fresnel scale (1.3 km) and over the exposure time of each data point (1 s, corresponding to about 7 km at Pluto) in order to be consistently compared to observations. The first figure uses the profile derived from Fig. 7A directly, while the second figure reduces the size of the temperature oscillations from the tidal calculations by a factor of 4. The first figure shows that the oscillations in the synthetic light curve are too large to match the observations, while reducing the atmospheric temperature oscillation amplitudes by a factor of about 3–4 (second figure) appears to be enough to match the light curve oscillations rather well.

the few quantities mentioned previously, the results appear very similar to the original surface N_2 ice distribution results shown in Figs. 3–8. This lack of sensitivity can be explained by the fact that the presence of at least one large-scale inhomogeneity in the distribution of ice at low latitudes will produce a large low-longitudinal wavenumber response.

5. Summary and conclusions

We have calculated one component of the dynamical activity expected in the atmosphere of Pluto. We find that the global atmospheric oscillations driven by diurnal sublimation “breathing” are predicted to produce wave-like patterns in the vertical thermal

structure similar to those inferred from stellar occultations. Vertical wavelengths derived from our tidal calculations are found to be approximately 7–12 km (Fig. 8), which are also in good agreement with observations (McCarthy et al., 2008; Person et al., 2008). Temperature oscillation amplitudes are also in reasonable agreement considering uncertainties in both modeling and observations. Observations have shown that temperature oscillations in Pluto's atmosphere are coherent over large horizontal distances, and our tidal calculations support this by showing dominance of low wavenumber modes. Furthermore the presence of N₂ ice on Pluto's surface implies that diurnally varying sublimation must be occurring. The tidal motions induced by sublimation are based on straightforward physics and we predict these tides are a major dynamical phenomenon on Pluto.

The tidal motions are in agreement with both McCarthy et al. (2008) and Person et al. (2008), who propose internal gravity waves and Rossby waves, respectively, to explain atmospheric perturbations. Both types of waves are present in the tidal solutions. The tidal modes are of gravity type for positive equivalent depths (related to eigenvalue, see Appendix A for details). These are the modes that propagate vertically. They include modes with horizontal scale spanning from the planetary radius down to frost patch dimensions. Their vertical scales are of order Ω/N times the horizontal scales, where N is the Brunt–Väisälä frequency. The Rossby modes are those with negative equivalent depths. In the present application they do not propagate vertically. Their amplitude is confined near the surface, where they play an important role in determining winds. The parameter determining the character of the atmospheric response is $NH/(\Omega a) \sim 7$, which is considerably larger than unity, leading to clean separation of the classes of modes (gravity waves vs. Rossby waves).

A discrepancy between this theory and the observations is that our standard low surface pressure case predicts amplitudes that are too large in comparison with those calculated from the occultations. This point of disagreement may be resolved by better determination of the surface pressure, since the prediction of wave amplitudes is inversely proportional to the magnitude of the surface pressure.

A weakness in the theory which may bear greater examination is the neglect of mean flows. The speed of the diurnally varying solar heating pattern on Pluto is approximately 10 m/s, and mean winds, if this large, would significantly alter the structure of the tides. Our calculations have assumed zero mean flow, which we feel is a reasonable assumption in the absence of observations indicating otherwise. It is difficult to ascertain with our present model whether the presence of mean flows may have the effect of equalizing the variation of wave amplitudes in latitude that the tidal model predicted but was not seen in the occultation data.

These tidal calculations make a prediction that can be verified or disproved with further observations. In particular, the theory predicts a variation in amplitude with latitude with largest amplitudes at low latitudes. The latitude coverage of observations is sparse and does not well define the latitude variations in wave amplitude. This is an important point to address with future observations.

In the present case, interaction of the stationary frost pattern and the westward-propagating solar heating gives rise to both eastward and westward tidal modes. The amplitude of these modes is particularly large at low latitudes. In this situation it is possible that a “Quasi-biennial Oscillation” phenomenon might be produced, with time-dependent zonal winds above the equator (Baldwin et al., 2001), but that is beyond the scope of the present paper.

Acknowledgments

We wish to thank Prof. Richard French and two anonymous reviewers for suggestions and improvements to the manuscript.

Appendix A. Tidal equations and method of solution

Here we provide a more detailed description of the equations and boundary conditions used in our tidal model as well as a brief description of the recipe we used to calculate our numerical solutions.

A.1. Tidal equations

The well-known linearized tidal equations for a thin atmosphere on a sphere are (Wilkes, 1949; Kato, 1966a,b; Chapman and Lindzen, 1970; Kasahara, 1976):

$$\frac{\partial u'}{\partial t} - 2\Omega v' \sin \phi = -\frac{1}{\rho_0 a \cos \phi} \frac{\partial P'}{\partial \lambda}, \quad (\text{A1})$$

$$\frac{\partial v'}{\partial t} + 2\Omega u' \sin \phi = -\frac{1}{\rho_0 a} \frac{\partial P'}{\partial \phi}, \quad (\text{A2})$$

$$\frac{\partial P'}{\partial z} = -g\rho', \quad (\text{A3})$$

$$\frac{\partial \rho'}{\partial t} + w' \frac{d\rho_0}{dz} + \rho_0 \chi' = 0, \quad (\text{A4})$$

$$\frac{\partial P'}{\partial t} + w' \frac{dP_0}{dz} = \gamma g H_0 \left(\frac{\partial \rho'}{\partial t} + w' \frac{d\rho_0}{dz} \right), \quad (\text{A5})$$

where the divergence, χ' , is given by

$$\chi' = \frac{1}{a \cos \phi} \left[\frac{\partial u'}{\partial \lambda} + \frac{\partial}{\partial \phi} (v' \cos \phi) \right] + \frac{\partial w'}{\partial z}. \quad (\text{A6})$$

The notation is standard. Spherical geometry is assumed, heating and friction are omitted, the atmosphere is assumed thin, and the rotation rate is Ω . The basic state profiles ρ_0 and P_0 are functions only of height. They are based on a mean temperature profile with a strong inversion within the lowest half scale height and a nearly isothermal middle atmosphere, as shown in Fig. 1. As mentioned in the caption to that figure, we have chosen to focus our analysis on numerical solutions using the low surface pressure since it yields the largest temperature perturbations. Differences between the two extreme cases were discussed in Section 5.

The horizontal boundary conditions are periodic in longitude and continuous at the poles. The vertical boundary conditions are the previously mentioned surface boundary condition, Eq. (3), and the assumption that no energy is reflected downward from the upper atmosphere. This assumption leads to an upper boundary condition on the tidal oscillations of the form:

$$\text{Evanescent modes: Amplitude} < \infty \text{ as } z \rightarrow \infty, \quad (\text{A7})$$

$$\text{Propagating modes: Energy flux} > 0 \text{ as } z \rightarrow \infty. \quad (\text{A8})$$

The tidal equations, Eqs. (A1)–(A6), can be combined to produce one single differential equation, which can then be solved by separation of variables into vertical and horizontal differential equations. If solutions are assumed to be a sum of different modes, then the separation constants become an infinite series of eigenvalues, whose corresponding eigenfunctions represent the modes in the sum.

In the case of free (i.e., unforced) oscillations (such as transient atmospheric waves), the eigenvalues are found by solving the vertical structure equation. These eigenvalues are then used in solving the horizontal structure equation, which for a specified longitudinal wavenumber, s , produces a unique frequency of oscillation for that wavenumber and eigenvalue.

In the case of forced oscillations (such as tides), the eigenvalues are found by specifying a longitudinal wavenumber, s , and frequency, σ , of oscillation of the forcing and then solving the horizontal structure equation for a series of eigenvalues. Each eigenvalue corresponds to a particular latitudinal function, called

a Hough function, Θ , in tidal theory, as a solution to the horizontal structure equation. The Hough functions are an infinite sum over associated Legendre polynomials, and thus are analytic functions whose coefficients in the infinite sum are merely functions of s , σ , and eigenvalue. In addition, each eigenvalue is also used to solve for a unique mode in the vertical structure equation. However, except in very special cases, these solutions are not analytic functions, and thus must be solved for numerically. The final solution is then a sum over all modes of the eigenvalues, for the specific forcing at longitudinal wavenumber, s , and frequency, σ , and convolving the horizontal Hough functions with the vertical structure solutions.

A.2. Method of solution

The presence of icy and non-icy N_2 patches introduces a spectrum of longitudinal wavenumbers to the surface forcing function. Examination of the power spectrum of the N_2 ice patch map (Fig. 2) revealed that there was significant power only in wavenumbers from -4 to 4 , where negative wavenumbers were used to preserve phase information. Using this longitudinal power distribution convolved with the diurnal insolation oscillation, we solved the tidal equations for one frequency, $\sigma = \Omega$, and for the range of longitudinal wavenumbers, s from -5 to 5 (to account for beating with the diurnal oscillation). Where astronomical parameters had seasonally-varying values (e.g., solar flux, solar declination, surface pressure, etc.) we chose to use values that corresponded with the time of the observations presented in Sicaudy et al. (2003), or mid-2002, and are listed in Table 1.

We did not limit our investigation to modes whose vertical wavelengths agreed with observations. Instead we used the longitudinal power spectrum of the surface albedo features in combination with the assumption of only a diurnal harmonic forcing frequency to calculate the tidal response.

The solutions to the tidal equations were calculated numerically. We followed the methodology of Kato (1966a,b) because he presented the clearest recipe for how to solve for eigenvalues given a particular forcing. Given an s and an f ($\equiv \sigma/(2\Omega)$), we used Eq. (3.14) of Kato (1966a) to find eigenvalues as zeroes of the function represented in that equation. The function is actually an infinite sum, but we truncated the sum at 40 terms, as including more terms did not significantly change the eigenvalues found. We used a standard published numerical root-finding algorithm, and searched for both positive and negative roots to the equation. Since finding the zeroes of this equation does not discriminate between the so-called “symmetric” and “antisymmetric” eigenvalues, we were able to correspond the largest absolute value eigenvalue (either positive or negative) as the first symmetric eigenvalue, and the next smallest (in absolute value) as the first antisymmetric eigenvalue. Further smaller (in absolute value) eigenvalues were then matched up as further symmetric or antisymmetric eigenvalues in alternating sequence. Typically, our root-finding algorithm found anywhere between 10 and 20 eigenvalues for a particular choice of s and constant choice of σ , which we deemed to be sufficient as smaller eigenvalues (in absolute value) contribute progressively less to the total solution when summed over all eigenvalues. The particular case of the $s = 0$, or zonally symmetric, component of the thermal tide presented a couple of difficulties. The leading terms in Eq. (3.14) used by Kato (1966a) are zero when $s = 0$. Thus we assumed that the continued fraction in the equation for the $s = 0$ case starts with the first non-zero term, $N_{s+1,s} - a_{s+1,s}/(\dots)$, and found eigenvalues for the zonally-symmetric tidal components as zeroes of the reduced equation.

Each eigenvalue in the forced tidal equation solution has a corresponding latitudinal profile function, the series of which are called Hough functions in tidal theory after Hough (1898) who first found

them, and which are individually a sum of associated Legendre polynomials in μ ($=\sin(\phi)$). The coefficients to the associated Legendre polynomials were found through Eqs. (3.16)–(3.19) of Kato (1966a), where we truncated the infinite series at 20 terms, as the coefficients rapidly approach zero with higher numbers of terms. Again, the particular case of the $s = 0$, or zonally symmetric, component of the thermal tide was a special case that needed to be dealt with. The recursion formula (3.16) of Kato (1966a) has a zero in the denominator at the first term, which we resolved by assuming that the coefficient of the first associated Legendre polynomial will be 0, which is reasonable as that associated Legendre polynomial is the constant, 1, and unnecessary to include in our expansion of oscillations. We assumed that the next coefficient in the sequence now started with a value of 1, and repeated the procedure as for other values of s , including renormalization of coefficients.

The horizontal shape of our solutions for a particular longitudinal wavenumber, s , to the forced equation will be a sum over all Hough functions (and thus all eigenvalues). The eigenvalues are also expressed traditionally as an “equivalent depth,” h_m , where

$$h_m \equiv \frac{4\Omega^2 a^2}{g} \delta_m, \quad (\text{A9})$$

and δ_m is the m th eigenvalue. The Hough function, $\Theta_m(\phi)$, is thus the Hough function corresponding to the eigenvalue δ_m , or equivalently, the equivalent depth h_m .

After finding all of the eigenvalues (positive and negative, symmetric and antisymmetric) for a particular longitudinal wavenumber, s , and the constant choice of frequency, σ , the vertical structure equation was then solved for each eigenvalue. Again, the recipe presented by Kato (1966b) was comparatively clear and straightforward, so we followed his methodology. The actual solution was also done numerically via a standard published tridimensional solver.

The differential equation for the vertical structure is of the form

$$\frac{d^2 y}{dx^2} + \left[-\frac{1}{4} + \frac{1}{h_m} \left(\frac{dH}{dx} + \frac{\gamma-1}{\gamma} H \right) \right] y = \frac{\gamma-1}{\gamma} \frac{q_m e^{-x}}{\gamma g h_m}. \quad (\text{A10})$$

The notation also follows Kato (1966b), where $\gamma = c_p/c_v$, $H = RT/g$ is the scale height, $x = \ln(P_s/P)$, h_m is the eigenvalue expressed as an equivalent depth via Eq. (A9), and y represents the scaled vertical structure function defined in Kato (1966a,b). We have assumed that radiative heating, which appears as q_m in the right-hand side of Eq. (A10), is essentially negligible for our purposes, and so the right-hand side of the equation is zero. The magnitude of the term multiplying y on the left-hand side of the equation we have called r^2 for convenience and defined it so that it will always be positive definite. Thus we may rewrite Eq. (A10) as

$$\frac{d^2 y}{dx^2} \pm r^2 y = 0, \quad (\text{A11})$$

$$r^2 = \left| -\frac{1}{4} + \frac{1}{h_m} \left(\frac{dH}{dx} + \frac{\gamma-1}{\gamma} H \right) \right|, \quad (\text{A12})$$

where the plus or minus sign appearing in front of r^2 in Eq. (A11) depends on the sign of r^2 before the absolute value is taken. It should also be noted that the term multiplying $1/h_m$ in Eq. (A12) is related to the buoyancy, or Brunt–Väisälä frequency, N , through the following relationship:

$$\frac{N^2 H^2}{g} = \frac{dH}{dx} + \frac{\gamma-1}{\gamma} H. \quad (\text{A13})$$

For Pluto, (most of the atmosphere (above a scale height or two) is nearly isothermal, and thus the scale height, H , and the change in scale height with altitude, dH/dx , in Eq. (A12) will both be nearly

constant. Thus, throughout most of the atmosphere (and particularly near the top), the solutions to Eq. (A11) will reduce to either exponentials or sines and cosines, purely depending on the sign of r^2 . Throughout most of Pluto's atmosphere, H is approximately constant since the atmosphere is nearly isothermal, and therefore dH/dx in Eq. (A12) is negligible. Thus, even the largest absolute values of the eigenvalues (which only get as large as order 10^{-1}), make the second term in Eq. (A12) much, much larger than $-1/4$. Thus the sign appearing in front of r^2 will depend purely on the sign of the eigenvalue, or equivalently, h_m , and the solutions to Eq. (A11) correspond rather readily to either evanescent or propagating modes merely according to the sign of the eigenvalue. That is, a negative eigenvalue corresponds to an evanescent mode, and a positive eigenvalue corresponds to a propagating mode. Thus, for the top boundary for negative eigenvalues, we imposed the following condition:

$$h_m < 0, \quad x \rightarrow \infty: \quad \frac{dy}{dx} + ry = 0, \\ r \equiv \sqrt{\frac{1}{4} - \frac{1}{h_m} \left(\frac{dH}{dx} + \frac{\gamma - 1}{\gamma} H \right)}, \quad (\text{A14})$$

where r is a positive, real number. This has the effect of removing increasing exponentials with height (roughly equivalent to the x variable) and keeping the vertical solutions bounded. For the top boundary for positive eigenvalues, we imposed the following condition:

$$h_m > 0, \quad x \rightarrow \infty: \quad \frac{dy}{dx} - iry = 0, \\ r \equiv \sqrt{-\frac{1}{4} + \frac{1}{h_m} \left(\frac{dH}{dx} + \frac{\gamma - 1}{\gamma} H \right)}, \quad (\text{A15})$$

where r is still a positive, real number and the other variables are as above. This boundary condition filters out upward propagating phase solutions, since for gravity waves the phase propagation direction is opposite to the energy flux direction, and our source of energy forcing is at the surface so we expect upward energy propagation and thus downward phase propagation.

The bottom boundary condition used was Eq. (3), where the physical vertical velocity variable, w , was converted into a function of the variable y used in the notation of Kato (1966b). This is Eq. (2.5) of Kato (1966b), where the terms on the left-hand side of the equation represent w written in terms of y . In our specification of $w(x = 0, \lambda, \phi, t) = w_S(\lambda, \phi, t)$, $M(\lambda, \phi)$, the frost map function, and $A(\lambda, \phi)$, the albedo, came from the data shown in Fig. 2. The function, F' , was approximated as:

$$F'(\lambda, \phi, t) = \frac{1}{2} F_{\odot} \cos \phi \cos \delta_{\odot} e^{i(\Omega t + \lambda - \pi)}. \quad (\text{A16})$$

F_{\odot} is the solar constant at Pluto's distance and δ_{\odot} is the declination of the Sun. The factor of one-half comes from approximating the time oscillation of the solar flux as varying about a non-zero mean, and thus the amplitude is about one-half the maximum value of the insolation. The factor of π in the exponential appears so that $t = 0$ represents local midnight at a longitude of 0° . The bottom boundary condition was then expressed as a sum of orthogonal Hough functions in order to create solutions to the vertical equation for each eigenvalue, i.e.,

$$w_S(\lambda, \phi, t) = \sum_{m=1}^{\infty} \sum_{s=-\infty}^{\infty} w_{m,s} \Theta_m(\lambda) e^{i(s\lambda + \Omega t - \pi)}. \quad (\text{A17})$$

In practice, m was summed to about 20 instead of ∞ , and s was summed from about -5 to 5 instead of $-\infty$ to ∞ . The coefficients $w_{m,s}$ were then found by projecting the source w_S function onto the orthogonal Hough functions and longitudinal and temporal sine waves, i.e.,

$$w_{m,s} = \frac{1}{2\pi} \int_{-\frac{\pi}{2}}^{\frac{\pi}{2}} \int_{-\pi}^{\pi} \frac{F_{\odot} \cos \delta_{\odot}}{2L\rho_s} \cos \phi \\ [1 - A(\lambda, \phi)] M(\lambda, \phi) e^{i\lambda} e^{i\Omega t} \Theta_m(\phi) e^{-is\lambda} d\lambda \cos \phi d\phi, \quad (\text{A18})$$

where the $1/2\pi$ pre-factor represents the normalization over longitude, and the normalization over latitude is already incorporated in the definition of Hough functions, which are orthonormal functions, i.e.,

$$\int_{-\frac{\pi}{2}}^{\frac{\pi}{2}} \Theta_m(\phi) \Theta_n(\phi) \cos \phi d\phi = \delta_{mn}, \quad (\text{A19})$$

where δ_{mn} is the Kronecker delta.

As mentioned in Section 4, the wavelengths that best match the observations arise from the lowest horizontal structure modes. That is, they have eigenvalues expressed in terms of equivalent depth of $h_m = 22.6$ m (the first positive, antisymmetric eigenvalue for wavenumber $s = 0$) and $h_m = 9.15$ m (the first positive, symmetric eigenvalue for wavenumber $s = -1$). Using Eq. (A12), with the assumption that the majority of the oscillations are occurring in the upper atmosphere where temperature is constant at around 100 K, to calculate the vertical wavenumber and then converting the result to height coordinates, these two equivalent depths yield wavelengths of 12 and 7.7 km, respectively, which very closely match observational values of dominant wavelengths of 12 and 8 km.

References

- Baldwin, M.P., and 14 colleagues, 2001. The Quasi-biennial Oscillation. *Rev. Geophys.* 39, 179–229.
- Chapman, S., Lindzen, R.S., 1970. *Atmospheric Tides – Thermal and Gravitational*. Gordon and Breach, 200pp.
- Elliot, J.L., and 28 colleagues, 2003. The recent expansion of Pluto's atmosphere. *Nature* 424, 165–168.
- Elliot, J.L., and 19 colleagues, 2007. Changes in Pluto's atmosphere: 1988–2006. *Astron. J.* 134, 1–13.
- Grundy, W.M., Buie, M.W., 2001. Distribution and evolution of CH_4 , N_2 , and CO ices on Pluto's surface: 1995 to 1998. *Icarus* 153, 248–263.
- Hansen, C.J., Paige, D.A., 1996. Seasonal nitrogen cycles on Pluto. *Icarus* 120, 247–265.
- Hough, S.S., 1898. On the application of harmonic analysis to the dynamical theory of the tides – Part II. On the general integration of Laplace's dynamical equations. *Philos. Trans. R. Soc. London* A191, 139–185.
- Kasahara, A., 1976. Normal modes of ultralong waves in the atmosphere. *Mon. Weather Rev.* 104, 669–690.
- Kato, S., 1966a. Diurnal atmospheric oscillation: 1. Eigenvalues and Hough functions. *J. Geophys. Res.* 71, 3201–3209.
- Kato, S., 1966b. Diurnal atmospheric oscillation: 2. Thermal excitation in the upper atmosphere. *J. Geophys. Res.* 71, 3211–3214.
- Kelley, M.C., Chen, C.Y., Beland, R.R., Woodman, R., Chau, J.L., Werne, J., 2002. Persistence of a Kelvin–Helmholtz instability complex in the upper troposphere. *J. Geophys. Res.* 110 (D14). doi:10.1029/2004JD005345.
- Lellouch, E., 1994. The thermal structure of Pluto's atmosphere: Clear vs. hazy models. *Icarus* 108, 255–264.
- Lellouch, E., Laureijs, R., Schmitt, B., Quirico, E., de Bergh, C., Crovisier, J., Coustenis, A., 2000. Pluto's non-isothermal surface. *Icarus* 147, 220–250.
- Lellouch, E., Sicardy, B., de Bergh, C., Käufel, H.-U., Kassi, S., Campargue, A., 2009. Pluto's lower atmosphere structure and methane abundance from high-resolution spectroscopy and stellar occultations. *Astron. Astrophys.* 495, L17–L21.
- Lide, D.R. (Ed.), 2008. *Handbook of Chemistry and Physics*, 89th ed. Chemical Rubber Company Press, 2736pp.
- Lodders, K., Fegley Jr., B., 1998. *The Planetary Scientist's Companion*. Oxford University Press, New York, 371pp.
- McCarthy, D.W., Hubbard, W.B., Kulesa, C.A., Benecchi, S.D., Person, M.J., Elliot, J.L., Gulbis, A.A.S., 2008. Long-wavelength density fluctuations resolved in Pluto's high atmosphere. *Astron. J.* 136, 1519–1522.
- Pasachoff, J.M., Souza, S.P., Babcock, B.A., Ticehurst, D.R., Elliot, J.L., Person, M.J., Clancy, K.B., Roberts, L.C., Hall, D.T., Tholen, D.J., 2005. The structure of Pluto's atmosphere from the 2002 August 21 stellar occultation. *Astron. J.* 129, 1718–1723.
- Person, M.J., and 18 colleagues, 2008. Waves in Pluto's upper atmosphere. *Astron. J.* 136, 1510–1518.
- Sicardy, B., and 40 colleagues, 2003. Large changes in Pluto's atmosphere as revealed by recent stellar occultations. *Nature* 424, 168–170.
- Stern, S.A., Buie, M.W., Trafton, L.M., 1997. HST high-resolution images and maps of Pluto. *Astron. J.* 113, 827–843.

- Strobel, D.F., Zhu, X., Summers, M.E., Stevens, M.H., 1996. On the vertical temperature structure of Pluto's atmosphere. *Icarus* 120, 266–289.
- Tholen, D.J., Buie, M.W., Grundy, W.M., Elliott, G.T., 2008. Masses of Nix and Hydra. *Astron. J.* 135, 777–784.
- Tryka, K.A., Brown, R.H., Cruikshank, D.P., Owen, T.C., Geballe, T.R., de Bergh, C., 1994. Temperature of nitrogen ice on Pluto and its implications for flux measurements. *Icarus* 112, 513–527.
- Wilkes, M.V., 1949. *Oscillations of the Earth's atmosphere*. Cambridge University Press. 74pp.
- Young, E.F., Galdamez, K., Buie, M.W., Binzel, R.P., Tholen, D.J., 1999. Mapping the variegated surface of Pluto. *Astron. J.* 117, 1063–1076.
- Young, E.F., Binzel, R.P., Crane, K., 2001. A two-color map of Pluto's sub-Charon hemisphere. *Astron. J.* 121, 552–561.